Improved Light Attenuation Method for 2D Data Acquisition of Sediment Depths

Jenn Wei Er[1], Adrian Wing-Keung Law[2], E. Eric Adams[3] and Yang Yang[4]

[1] Research Fellow, School of Civil and Environmental Engineering, Nanyang Technological University, 50 Nanyang Avenue, 639798 Singapore. Email: jwer@ntu.edu.sg

[2] Associate Professor, School of Civil and Environmental Engineering, Nanyang Technological University, 50 Nanyang Avenue, 639798 Singapore. Email: cwklaw@ntu.edu.sg

[3] Senior Research Engineer and Senior Lecturer, Department of Civil and Environmental Engineering, Massachusetts Institute of Technology, Cambridge, MA 02139, USA. Email: eeadams@mit.edu

[4] Undergraduate Student, School of Civil and Environmental Engineering, Nanyang Technological University, 50 Nanyang Avenue, 639798 Singapore. Email: yang0383@e.ntu.edu.sg

Abstract

An improved light attenuation method (LAM2D – Light Attenuation Method for Two-Dimensional Data Acquisition) to quantify two-dimensional (2D) sediment depths with higher accuracy is developed in the present study. The working principle is to relate attenuated light intensities with depths of the sediment layer. Traditionally, calibration has been performed with the scraper method with either multiple constant depth sediment profiles or a slope with incremental depth profile. This method works well for coarse sediment, but is shown to be inaccurate for fine sediment with shallow sediment depth in the near-zero limit regime. In the present study, a new method is established for the calibration of shallow sediment depth by utilizing the correlation of particle plume deposition profiles. The practical application of

LAM2D to determine sediment deposition profiles from a laboratory simulation of barged sediment disposal was demonstrated with both approaches. The errors in the overall determination of sediment mass were found to be significantly reduced with the current approach.

Introduction

In the laboratory study of sediment transport, environmental hydraulics and coastal engineering, the investigation of sediment deposition and bathymetry changes require the accurate measurements of sediment distribution over the affected area. Previous measurement techniques to achieve this objective had been summarized in details by Munro and Dalziel (2005). They included the ultrasonic depth profiler and stereo-photography which have limited spatial resolution, and also the laser three-dimensional (3D) scanner which has high accuracy but is expensive with long acquisition time (Lague et al. 2003). Alternatively, Rooij et al. (1999) employed an array of electrodes on the bottom of the tank to determine the sediment depth based on the resistance induced through the sediment layer. This method enables real time measurements, but is limited by the range of sediment depths as the voltage signal quickly saturates in a deep sediment layer. In addition, the measurement extent is restricted by the coverage of the electrodes. Munro et al. (2004) developed a novel technique by comparing the reference image (image of undisturbed sediment layer) with the new image after the redistribution of sediment particles. Through a pattern-matching algorithm, high-resolution particle redistribution measurements were obtained. However, this technique was found to be impractical in terms of real time measurements. Subsequently, Munro and Dalziel (2005) proposed instead a light attenuation method (LAM) to resolve the temporal displacement of particles, which shall be reviewed in details in the following.

Light attenuation methods have been successfully applied to a wide range of studies involving single-phase flows. Holford and Dalziel (1996) used this method for the visualization and quantification of baroclinic instability of a two-layer rotating fluid system. Cenedese and Dalziel (1998) and Kikkert (2006) applied LAM to measure the depth-averaged concentration of a single-phase buoyant convective flow. Besides single-phase flows, LAM had also been used to investigate two-phase flows (i.e. air-water, solid-water flows), e.g. measuring the void fraction of micro bubbles (Leppinen and Dalziel 2001), gravity currents (Yuan et al. 2011), and the particle displacement or deposition in aqueous environments (Munro and Dalziel 2005; Sutherland and Dalziel 2014).

A potential additional application of LAM includes the measurement of oil spill thickness. The thickness of oil slicks can range from 0.1 μm to 10 mm (Fingas and Brown 2014). Several techniques have been employed by using acoustic wave, infrared, laser, radar, light (reflection or refraction) and visual inspection. The quantification of oil spreading thickness from the attenuation of backlighting is worth exploring, but the preparation of calibration samples is a challenge. The technique in LAM2D can be applied to generate the desired and accurate oil thicknesses for calibration. Another application for laboratory study is to determine the concentration of suspended sediments (e.g., in a sediment thermal or sediment clump). The calibration curve can be obtained by using a particle plume (or jet) with known concentration distribution (Azimi et al. 2011), and measuring the attenuated light intensity across the plume (or jet). The existing calibration method used a container filled with sediment-water mixture, and recorded the attenuated intensity (Wu et al. 2014). This process was repeated by changing the concentration of sediment in the mixture until a curve was obtained. The limitations of the existing method are that it is time consuming and the container must have the same width as the model tank.

In terms of measuring sediment depths, the principle of LAM involves the attenuation of light intensity transmitted through the sediment layer, and the sediment depth is then determined based on the attenuated intensity. In this case, the two most important parameters are the reference (I_{ref}) and attenuated (I) intensities without and with the presence of the sediment layer, respectively (Fig. 1). Upon transmitting through the sediment layer, the incident light is absorbed and reflected/refracted. The transmission ratio can be calculated as the ratio of attenuated intensity to the incident intensity. Nine ratios between 0 and 1 can be identified to account for the absorption (i.e. C_a, C_w, C_g, C_p) and reflection/refraction losses (i.e. $C_{a\text{-}g}$, $C_{g\text{-}w}$, $C_{w\text{-}a}$, $C_{g\text{-}p}$, $C_{p\text{-}w}$). The subscripts *a*, *g*, *w* and *p* represent the media of air, glass, water and particles, respectively. The interfaces between the media are noted with hyphen (-). Thus, I_{ref} can be expressed in the following equation (Kikkert 2006):

$$I_{ref} = C_a \times C_w \times C_g \times C_{a\text{-}g} \times C_{g\text{-}w} \times C_{w\text{-}a} \times I_{source} \quad (1)$$

where I_{source} is the source intensity, while I can be represented as

$$I = C_a \times C_w \times C_g \times C_{a\text{-}g} \times C_{g\text{-}w} \times C_{w\text{-}a} \times C_p \times C_{g\text{-}p} \times C_{p\text{-}w} \times I_{source} \quad (2)$$

Hence,

$$I/I_{ref} = C_p \times C_{g\text{-}p} \times C_{p\text{-}w} \quad (3)$$

Thus, the ratio of attenuated to reference intensity is dependent on the characteristics of the particles (i.e. h_s and d_{50}, where h_s is the sediment depth and d_{50} is the median particle size). Equation (3) can be formulated as

$$I/I_{ref} = f(h_s, d_{50}) \quad (4)$$

with each particle size having its own unique calibration curve, and the same type of particle shall be used for both the calibration and actual tests. It should be noted that the formulation of Equations (1) to (4) might vary depending on the experimental apparatus and the features of the target to be measured.

Previous Calibration

Calibration is required to establish the functional form of Equation (4) (i.e. calibration curve). Munro and Dalziel (2005) used sediment particles with d_{50} = 0.25 mm, and prepared calibration profiles by scraping the sediment to a constant depth or a linearly slope depth and measuring the attenuated intensity, *I*, of the profiles. The scraping method worked adequately for sediment depth h_s > 2 mm or h_s/d_{50} > 8 if d_{50} = 0.25 mm. By plotting the normalized attenuated intensity, I/I_{ref} with the sediment depth, h_s/d_{50}, they observed an exponential decay when h_s/d_{50} > 18 as expected from Beer-Lambert's law, and called this region the self-similar regime. An exponential fit of the data was performed in this regime as

$$\frac{I}{I_s} = \exp\left\{ b\left(\frac{h_s - h_c}{d_{50}} \right) \right\}, \; h_s > h_c \tag{5}$$

where I_s is the intensity at $h_s = h_c$, where h_c is the critical h_s determined to be $18d_{50}$, and β is the empirical coefficient. The regime with h_s/d_{50} < 18 was termed the near-zero limit regime, and the attenuation did not follow Beer-Lambert's law. In this regime, they performed a least square fit with the following equation chosen for empirical convenience:

$$\frac{I}{I_{ref}} = \exp\left\{ a\left(\frac{h_s}{d_{50}} \right)^{g} \right\} \tag{6}$$

where α and γ are the empirical coefficients that fitted with all the data (including the data in self-similar regime) but constrained to I/I_{ref} = 1 at h_s/d_{50} = 0 and $I/I_{ref} \rightarrow 0$ when $h_s/d_{50} \rightarrow \infty$. Overall, the calibration profiles prepared by Munro and Dalziel (2005) were appropriate for coarse sediments (i.e. large d_{50}) as a wide range of h_s/d_{50} (from near-zero limit to self-similar regimes) could be covered.

Our focus on the further development of the LAM method in this study stemmed from our ongoing interest related to the deposition of sediment clouds occurring during open water barged sediment disposal (Er et al. 2016). Typically, the sediment size used in our laboratory

experiments was approximately 0.12 mm (fine to very fine sand) as determined from Froude scaling of field grain sizes (Wang et al. 2015), whereby a small value of h_s (< 2 mm) would be expected based on preliminary experimental observations. Hence, although the range of h_s/d_{50} might be similar to that in Munro's study (from near-zero limit to self-similar regimes), the values of h_s that needed to be determined were much shallower (since finer d_{50} was used) and could not be suitably prepared using the scraper method.

In the present study, an improved light attenuation method (LAM2D) is established, which uses different techniques to prepare the calibration curves. For deeper h_s (h_s > 2 mm), the traditional scraping method was used. For shallower h_s (h_s < 2 mm), however, an innovative technique using the deposition profiles produced by a particle plume which had small and measurable h_s was used instead. The calibration curves in the two regimes were established solely with data collected in the respective regime. This improved technique would benefit laboratory experiments that involve shallow sediment depth or those in which the change in sediment depth between pre- and post-tests is small. In the following, the experimental setup, particularly the novel calibration technique developed to calibrate the shallow h_s, is first presented. This is followed by the application of LAM2D to the measurement of deposition profiles from barged sediment disposal, and examination of the improvement over previous approach.

Experimental Setup

In the present study, the experiments were conducted in a 2 m (long) × 0.9 m (high) × 0.85 m (wide) water tank. The bottom of the tank was constructed with transparent glass to facilitate backlighting. Fresh water was used as the ambient fluid with water depth, h = 10 cm. Uniform-size particles (Ballotini Impact beads, Potters Industries, Inc.) with a density, ρ_s of 2.5 g/cm^3 and size, d_{50} of 0.12 mm were used as the sediment particles for most of the experiments. The

particle size ranged from 0.09 to 0.15 mm with the size distribution being determined by Chow (2004) using sieve analysis.

Light Attenuation System

Light Panel

Fourteen 1.5 m (~5 ft.) long T8 fluorescent tubes were arranged equidistantly covering a width of 0.85 m in an aluminum rectangular box. The panel was placed horizontally under the glass tank facing upward as shown in Fig. 1. Several light sources were considered during the design stage, and fluorescent tubes were finally chosen because the light is emitted in a radial manner as compared to light-emitting diode (LED) light which is directional, and it has lesser variation with respect to intensity than halogen and overhead projector (OHP) lights (Kikkert 2006). The generation of a uniform light source over the measurement domain was a key issue in the current setup. To achieve this condition, the box cover was fabricated with light diffuser material (acrylic diffusion sheet). By increasing the panel depth (the distance between tubes and diffusion sheet), the uniformity of the light source could be greatly enhanced. In addition, the inner frame of the box was painted with highly reflective paint to promote reflections and improve the uniformity of the light at the edges of the box.

Before the experiments, the light panel was tested for light uniformity as well as consistency over short (i.e. within an hour) and intermediate (i.e. within weeks) periods of time. The results showed that the light panel was able to produce a uniform light source with a low coefficient of variance, CV ≈ 1.6 % over an areal domain of 1.0 m × 0.5 m, which was sufficient to determine the deposition profiles from barged sediment disposal in the present experiments. Due to the temperature dependence of the fluorescent tube, the light intensity was expected to change over time as the temperature increased with prolonged test duration. The variation of intensity over time was recorded and observed to be stable between 20 to 40 minutes after the

light panel was switched on. Note that, the users should examine their light panel beforehand to reduce the experimental uncertainty induced by the variation of background light intensity.

Camera

A Nikon D700 DSLR (Digital Single-Lens Reflex) camera with a color CMOS (complementary metal-oxide semiconductor) sensor, equipped with a zoom lens (AF-S Zoom-Nikkor 24-70mm f/2.8G ED) was employed in the setup. The camera was mounted on top of the water tank, facing vertically downward toward the light panel. The distance between the camera and the measurement domain (sediment profile) was adjusted to achieve a balance between the needs to reduce the barrel distortion (i.e. increase in the distance between camera and target) and to retain a good resolution (i.e. decrease in the distance between camera and target). Finally, it was determined that the optimal distance was for the camera to be placed 1 m above the bottom of the tank. Each pixel in the captured images corresponded to an area of 0.34 mm × 0.34 mm.

Previous studies typically used a CCD (charge-coupled device) camera with a global shutter for the image capturing. Comparatively a CMOS camera usually operates with a rolling shutter (Konz et al. 2009; Njifenju et al. 2013). Due to the functional principle of the rolling shutter, the issue of flicker intensity was expected (Yoo et al. 2014) and the flickering was also observed in the current setup. To mitigate this issue, the camera exposure time, t_c was increased to average over the flickering light bands. With the current light panel, $t_c > 1/40$ was found to be sufficient. Besides the exposure time, other parameters such as the *f*-stop (f/n), ISO sensitivity and white balance were adjusted to achieve I_{ref} in a range of 240 ~ 250 (8 bits per pixel, giving integer intensity levels of $0 \leq I \leq 255$). The selection criteria for each parameter are listed in Table 1. The final set of parameters chosen was: $t_c = 1/30$, ISO = 400 and $f/n = f/22$ with 26 mm field of view. The same set of parameters and format of images should be used during both the calibration and actual tests.

With the color sensor, three-color signals (red, green and blue) were recorded and analyzed. From the results, the blue signal attenuated the most and hence yield the best intensity resolution for the calibration curves. In the subsequent analysis, the intensities ($I_{b\ ref}$ for the reference intensity and I_b for the attenuated intensity of the blue signal) were reported and analyzed.

Calibration Experiments

The calibration approach established in the new method required two different calibration experiments, one for the deep and one for the shallow h_s with 2 mm being the critical changeover value. For deep h_s (h_s > 2 mm), the traditional scraping technique was used with multiple constant sediment depths. As our water tank was large, scraping the sediments over the entire bottom was impractical. A set of rings (termed calibration rings) with constant height (2 mm) was used instead, and the sediment was scraped within the rings. The ring height was subsequently increased to 4 and 6 mm by stacking up two or three rings, respectively. Another technique discussed in the literature was to scrap the sediments along a constant slope was also attempted. However, we found that the lateral sediment profiles were uneven with this technique when approaching small h_s. Moreover, the profiles near this region were highly sensitive to the disturbance.

For shallow h_s (h_s < 2 mm), the correlation of particle plume deposition profiles from two test types was implemented instead. The two test types were: (i) the depth distribution profile (h_s vs. r_m, where r_m is the radius measured from the center of the profile) obtained from manual collection experiments (Test MC); and (ii) the attenuated intensity profile (I vs. r_m) measured from the light attenuation experiments (Test LA). In Test MC, the collection method described by Gensheimer et al. (2012) to quantify the deposition of sediment clouds released in ambient currents was applied; the procedure will be discussed in more detail in the next section. In each

case, the deposition profiles were generated by releasing a fixed amount of particles from a funnel with a round opening. After the release from the opening, the gravity-driven particle plume descended through the water column and expanded laterally due to entrainment. Upon impact on the bottom, the particle plume spread horizontally as a gravity current before depositing. The dynamics of descent and deposition of the particle plumes were similar to that of the sediment clouds from barge disposal and hence gave an additional motivation for this calibration in our study.

Note that the same sediment profile could not be used for the two test types (i.e. Tests MC and LA). This was because Test MC required the grids to be printed on the platform/tank to guide the quantification process, while Test LA required the sediment to be deposited on a tank clear from marking for better illumination and measurement. Two important criteria were needed for the generated profiles for calibration: (i) consistent and high repeatability, and (ii) axisymmetry, so that the depth distribution could be presented as an azimuthal mean depth profile for analysis to reduce the local variation. Finally, the calibration curve was determined by correlating the results from these two test types.

Two calibration tests with a total 10 replicates were conducted by adopting the same release conditions. Table 2 summarizes the test conditions. In Test MC, the sediments were manually collected, dried and weighted to determine the depth distribution profile. On the other hand, Test LA measured the attenuated intensity profiles with the light panel. In the following sections, the apparatus and test conditions of the particle plume deposition experiments will be discussed in detail.

Particle Plume Experiments

The particle plumes were generated by continuously releasing a mass of 10 g of sediment from a funnel with an opening radius of 5 mm. The sediment deposited on a platform with circular

grids printed, as shown in Fig. 2. Each replicate included the cumulative of five 10 g releases to increase the volume of deposited sediment and hence minimize the local variation. In a preliminary study, several alternative release mechanisms were considered, but they were all found to be inadequate. For example, the quasi-instantaneous release of the same mass (i.e. 10 g) of sediment using a cylindrical tube with bigger opening (9 mm radius) that was sealed with a layer of latex membrane (Zhao et al. 2014) produced highly inconsistent deposition profiles, possible due to the formation of sediment clumps.

The 10 cm water depth was measured from the platform to the water surface. After five releases, the water was slowly drained out from the tank to keep the deposition profiles undisturbed. The sediment layer was then left over night until the excess water was evaporated before removing it from the glass tank. Subsequently, the sediment deposited within the same circular grid interval was collected with a brush, dried in an oven for two hours at 130 °C and weighed. The mass distribution (m_s vs. r_m, where m_s is the mass of sediment) was converted to depth distribution (h_s vs. r_m) using the following equation:

$$h_{si} = \frac{V_{si}}{A_i} \text{ with } V_{si} = \frac{m_{si}}{r_s(1 - n)} \tag{7}$$

where the subscript i represents the i-th ring from the center of the circular grid (release point), V_{si} is the volume of sediment, A_i is the area of ring, and n is the void ratio, which was assumed to be a constant $n = 0.44$ based on our previous study (Zhao et al. 2012).

In Test LA, before releasing the sediment, the reference intensity, I_{ref} was measured for each replicate to check for consistency and then used for the normalization of I. Afterward, particle plumes with the same release conditions as Test MC were released and deposited directly on the bottom of the glass tank (Fig. 3). After five releases, the attenuated intensity profile using the light panel, I vs. r_m, was determined.

Results

In this section, the sediment depth distribution and attenuated intensity profiles of the deposition of particle plumes are discussed. The comparative results are then used to establish the calibration curves for both regimes. Improvements of current approach over the previous approach (using scraper method only) are also shown.

Particle Plume Deposition Profiles

The radial distributions of the mean depth profiles from Test MC are plotted in Fig. 4, with r_m = 0 being the center of the funnel. Only three profiles are presented for brevity. When the experiment was initiated, the sediment particles were observed to descend continuously from the opening with a 'thermal-like' front head. The particle cloud had a typical tadpole shape, similar to the buoyant starting plume observed by Ai et al. (2006). Upon impact with the bottom, the momentum of the 'thermal-like' front head and the density difference (buoyancy) drove the collapsed plume to propagate radially as gravity current. The sediment particles then gradually settled out from the gravity current as it propagated away from the release point. With the current test conditions, ~ 35 % of the particle deposited in the area within r_m < 4 cm and ~ 60 % deposited outside the ring area with r_m > 4 cm. The remaining particle (< 5 %) propagated and settled outside the test region (i.e. r_m > 18 cm). By comparing the profiles in Fig. 4, the variation among the replicates was found to be very small, which was attributed to the careful handling which minimized human errors during the measurement process and randomness in the releases.

Fig. 5 illustrates the attenuated intensity profiles from Test LA normalized by the reference intensity, $I_{b\,ref}$. In contrast, Munro and Dalziel (2005) normalized I (p,q) by I_{ref} (p,q) recorded at the beginning of each test, where p and q denote the row and column vectors of the pixel matrix. The pixel-by-pixel normalization could be achieved only when the camera and tank

were stationary from pre- to post-tests. In the current experimental setup, the camera had to be moved for the installation of the funnel or the model barge. Hence, the pixels were not exactly aligned in the images between pre- and post-tests. In this case, the normalization had to be done with a mean intensity produced by a uniform light source. From Fig. 5, it is noted that the attenuation profile had a similar distribution pattern as the sediment depth profile measured from Test MC (Fig. 4). The variation among the replicates was also insignificant as shown from the plotted error bars.

Calibration Curves

A piece-wise continuous calibration curve was established for the current approach and presented in Fig. 6, with the solid and dashed lines representing the curve in near-zero limit and self-similar regimes, respectively. A break in the curve at h_s/d_{50} = 16.7 can be identified which agrees well with the critical h_s/d_{50} (h_c/d_{50} = 18) found by Munro and Dalziel (2005) using the scraper method. It could be argued that the agreement was coincidental because, for our chosen d_{50} = 0.12 mm, the break point at h_s/d_{50} = 16.7 occurred at a value of h_s = 2 mm which was also the dividing line between the scraper method and sediment deposition method. To verify that the critical value of h_s/d_{50} was associated with light attenuation rather than the method of profile generation, several supplemental tests (Test ETs) were carried out using larger values of d_{50} as summarized in Table 3. The results are shown in Fig. 7 and again the break in calibration curves occurred at $h_s/d_{50} \sim 18$ (vertical dotted line), which was close to the h_c/d_{50} discussed above.

The effect of shallowness is illustrated in Fig. 8, with Fig. 8(a) showing the transmission of light through a single particle. Due to the spherical shape, the attenuation of light is greater in the center and weaker at the sides. When the light is passing through a layer of particles with h_s/d_{50} = 2, the packing of particles is important as illustrated in Fig. 8(b) and (c). However, the

packing of particles is less important for thick sediment layer ($h_s >> d_{50}$) as every light ray needs to transmit through similar layers of particles. The attenuation of light may not be uniform when the sediment layer is shallow. In this study, the particles are randomly packed and averaged values are used. Overall, the results in Fig. 7 suggested that the break in the calibration curve was due to the physics of light transmission as discussed above rather than the profile generation method.

From Fig. 6, in the self-similar regime, the data (filled markers) were measured from the calibration rings (scraper method) with three or five replicates. As expected, the attenuation followed the Beer-Lambert's law and experienced an exponential decay with the following equation:

$$\frac{I_b}{I_{b\ ref}} = c \exp\left\{-k_1\left(\frac{h_s}{d_{50}}\right)\right\} \tag{8}$$

where c and k_1 were determined to be 0.966 and 0.027, respectively from the least-square fit.

In the near-zero limit regime, the data (open markers) were determined by correlating the two profiles discussed in the previous section (i.e. h_s/d_{50} vs. r_m and $I_b/I_{b\ ref}$ vs. r_m to generate $I_b/I_{b\ ref}$ vs. h_s/d_{50}). Here, two regions in the depth distribution profile (h_s/d_{50} vs. r_m) were identified: (i) the region with $h_s < d_{50}$, within which the area was not fully covered by the sediment particles and (ii) $r_m < 4$ cm, where the gradient of h_s (dh_s/dr_m) was steep and current grid space was insufficient to accurately acquire the depth profile in this region. Therefore, the results in these regions were not included.

Fig. 6 suggests that the attenuation is linearly proportional to h_s/d_{50}, and can be expressed as

$$\frac{I_b}{I_{b\ ref}} = a + b\left(\frac{h_s}{d_{50}}\right) \tag{9}$$

where a (= 1) is constrained to yield $I_b/I_{b\,ref} = 1$ at $h_s/d_{50} = 0$ and b was determined to be -0.023 from the least square fit. The calibration curve is only applicable down to $h_s/d_{50} = 1$ (i.e. $I_b/I_{b\,ref} = 0.977$), below which the pixel area is not fully covered by sediment.

As discussed earlier, in the previous approach, the curve was established from the scraper method and fitted with

$$\frac{I_b}{I_{b\,ref}} = \exp\left\{-k_2\left(\frac{h_s}{d_{50}}\right)^{\gamma}\right\} \tag{10}$$

constraining to $I_b/I_{b\,ref} = 1$ at $h_s/d_{50} = 0$ and $I_b/I_{b\,ref} \rightarrow 0$ when $h_s/d_{50} \rightarrow \infty$ (Munro and Dalziel 2005), with $k_2 = 0.029$ and $\gamma = 1$ obtained from the collected data. Fig. 9 compares the calibration curves in the near-zero limit regime established from current (solid line) and previous (dashed line) approaches. The variation in the measurements of h_s/d_{50} with the present approach was primarily within the range of 0 to 1.2.

Application – Deposition of Barged Sediment Disposal

Activities such as dredging (with associated dredged material management) and land reclamation often involve open water sediment disposal. A barge is commonly used to transport and dispose of the sediments due to its large carrying capacity. From field observations, Bokuniewicz et al. (1978) identified three phases of the sediment transport upon release: (i) convective descent phase, during which the flow behavior is dominated by the disposal conditions and driven by gravity, (ii) bottom collapse phase, during which the disposed sediments impact the seabed and begin to spread horizontally, and (iii) passive-transport dispersion phase, when the sediments are passively carried by the ambient currents and turbulence.

In the present study, the laboratory investigation of barged sediment disposal was conducted in the same water tank, with the same water depth (h = 10 cm) as the calibration

357 tests. A model barge (shown in Fig. 10, made with two rectangular acrylic boxes) was designed
358 from an actual barge scaled down to dimensions of 20 cm (length, L) × 4 cm (width, W_b) × 4
359 cm (depth, D_b). Once the experiment was initiated, the two rectangular boxes would rotate in
360 opposite directions with an angular speed, ω, forming an opening (opening width, W = 0.8 and
361 0.5 cm) in the middle through which the sediment was released. The attenuated intensity profile
362 of the deposited sediment was taken from a single release of 112 g of sediment particles
363 (Ballotini Impact beads, d_{50} = 0.12 mm).

364 Upon release, the sediment cloud would descend through the water column and grow in
365 lateral size due to entrainment. Upon impact with the bottom, gravity currents would be
366 initiated by the cloud buoyancy to propagate horizontally, as illustrated in Fig. 11. In contrast
367 to the deposition from a funnel with an axisymmetric round opening, the rectangular opening
368 of the model barge created a nearly elliptical deposition pattern with the major axis
369 perpendicular to the barge, as presented in the last photo of Fig. 11. This was due to the fact
370 that the gravity current initiated by the two-dimensional starting plume, as predicted by BSDM
371 (Barged Sediments Disposal Model) (Er et al. 2016) based on the present release parameters,
372 grew primarily in the transverse direction (x-axis).

373 Figs. 12 and 13 illustrate the sediment depth profiles determined from current (symbols)
374 and previous approaches (lines) at various cross sections for the two tests with L/W = 24 and
375 40, respectively. The spreading behavior of the gravity currents along the azimuthal direction
376 could be explained by comparing the longitudinal profiles (h_s vs. x) at different y-locations.
377 The gravity currents had the highest spreading near the center of the barge (y = 0 cm), and
378 weakened when approaching the edge of the barge (y = 10 cm). This might be attributed to the
379 minor longitudinal spreading and shear force exhibited on the boundaries of the gravity current.

380 In general, both approaches were able to capture the spreading behavior of the gravity
381 currents. However, the maximum sediment depths and horizontal extents of the deposition

profiles determined from the previous approach were smaller than those of LAM2D. For instance, in the test with L/W = 24, measurement from LAM2D showed that the deposition profiles at y = 10 and 12 cm could reach a maximum of x = 15 and 10 cm, respectively. However, the previous approach yielded contracted profiles with the maximum x-direction extent at these two cross sections being only 5 and 10 cm, respectively. Moreover, based on the transverse profiles (h_s vs. y), the previous approach failed to capture the sediments that deposited beyond x = 20 cm. Similar conclusions could be drawn when comparing the profiles from the test with L/W = 40. Most importantly, the total mass conservation errors, ε_t from LAM2D ($\varepsilon_{t\ \mathrm{cur}}$ = – 9.6 % and – 9.8 % for L/W = 24 and 40, respectively) were significantly less than those of the previous approach ($\varepsilon_{t\ \mathrm{pre}}$ = – 24.4 % and – 21.9 % for L/W = 24 and 40, respectively). These differences in mass conservation errors between previous and current approaches are significant when compared with the less than 2 % sediment loss in an experiment. We could account for 98.4 % of the mass within our measurement domain with the remaining 1.6 % presumably being transported downstream. The mass conservation error would generally be negative because some sediment inevitably fell outside the domain. The reduction in error can be directly attributed to the improved calibration in the near-zero limit regime with the present approach.

Conclusions

An improved light attenuation method (LAM2D) was developed in this study using a CMOS camera and analyzing the blue signal. The approach method used different calibration techniques for the two ranges of deep and shallow sediment depths, with the traditional scraper method and the correlation of particle plume deposition profiles (depth distribution and attenuated intensity profiles), respectively. The calibration curve for each was established with data only in the respective range to better represent the attenuation behavior. The improved

method (LAM2D) was shown to reduce the mass conservation error significantly for shallow sediment depth (near-zero limit regime), compared with the previous approach with calibration based only on the scraper method.

LAM2D, or the light attenuation method in general, has two caveats: (i) the light panel needs to perform consistently throughout the test, and (ii) changing the setup, i.e. type of sediment particles, camera or light panel, requires re-calibration. There is also a challenge to use poly-dispersed particles in LAM as the attenuation varies with particle sizes as illustrated in Figs. 6 and 7. However, the poly-dispersed particles could be represented with an equivalent particle size to obtain the calibration curve. It should be mentioned that most laboratory applications use mono-dispersed, or nearly mono-dispersed particles, lessening the complications associated with variable grain sizes. With the appropriate adjustment of the calibration technique, we expect LAM2D could be useful in related applications such as the measurement of the thickness of oil spreading on the water surface and the quantification of the suspended sediments concentration in the water column.

Acknowledgements

This research was supported by the National Research Foundation Singapore through the Singapore MIT Alliance for Research and Technology's Center for Environmental Sensing and Modeling interdisciplinary research program.

References

Ai, J. J., Law, A. W. K., and Yu, S. C. M. (2006). "On Boussinesq and non-Boussinesq starting forced plumes." *Journal of Fluid Mechanics*, 558, 357–386.

Azimi, A. H., Zhu, D. Z., and Rajaratnam, N. (2011). "Effect of particle size on the characteristics of sand jets in water." *Journal of Engineering Mechanics*, 137(12), 822–834.

Bokuniewicz, H. J., Gebert, J., Gordon, R. B., Higgins, J. L., and Kaminsky, P. (1978). *Field Study of the Mechanics of the Placement of Dredged Material at Open-Water Disposal Sites.* Technical Rep. D-78-7, U.S. Army Engineer Waterways Experiment Station, Vicksburg, MS.

Cenedese, C., and Dalziel, S. B. (1998). "Concentration and depth fields determined by the light transmitted through a dyed solution." *8th International Symposium on flow visualisation*, Sorrento, Italy.

Chow, A. C. H. (2004). "Effects of buoyancy source composition on multiphase plume behavior in stratification." Massachusetts Institute of Technology.

Er, J. W., Law, A. W. K., Adams, E. E., and Zhao, B. (2016). "Open water disposal of barged sediments." *Journal of Waterway, Port, Coastal, and Ocean Engineering*, 142(5), 4016006.

Fingas, M., and Brown, C. (2014). "Review of oil spill remote sensing." *Marine Pollution Bulletin*, 83(1), 9–23.

Gensheimer, R. J., Adams, E. E., and Law, A. W. K. (2012). "Dynamics of particle clouds in ambient currents with application to open-water sediment disposal." *Journal of Hydraulic Engineering*, 139(2), 114–123.

Holford, J., and Dalziel, S. (1996). "Measurements of layer depth during baroclinic instability in a two-layer flow." *Applied Scientific Research*, 56(2–3), 191–207.

Kikkert, G. (2006). "Buoyant jets with two and three-dimensional trajectories." University of Canterbury.

Konz, M., Ackerer, P., Huggenberger, P., and Veit, C. (2009). "Comparison of light transmission and reflection techniques to determine concentrations in flow tank experiments." *Experiments in Fluids*, 47(1), 85–93.

Lague, D., Crave, A., and Davy, P. (2003). "Laboratory experiments simulating the geomorphic response to tectonic uplift." *Journal of Geophysical Research: Solid Earth*, 108(B1), ETG 3-1-ETG 3-20.

Leppinen, M. D., and Dalziel, S. B. (2001). "A light attenuation technique for void fraction measurement of microbubbles." *Experiments in Fluids*, 30(2), 214–220.

Munro, R. J., and Dalziel, S. B. (2005). "Attenuation technique for measuring sediment displacement levels." *Experiments in Fluids*, 39(3), 602–613.

Munro, R. J., Dalziel, S. B., and Jehan, H. (2004). “A pattern matching technique for measuring sediment displacement levels.” *Experiments in Fluids*, 37(3), 399–408.

Njifenju, A. K., Bico, J., Andrès, E., Jenffer, P., and Fermigier, M. (2013). “Experimental investigation of liquid films in gravity-driven flows with a simple visualization technique.” *Experiments in Fluids*, 54(5), 1–9.

Rooij, F. D., Dalziel, S. B., and Linden, P. F. (1999). “Electrical measurement of sediment layer thickness under suspension flows.” *Experiments in Fluids*, 26(5), 470–474.

Sutherland, B. R., and Dalziel, S. B. (2014). “Bedload transport by a vertical jet impinging upon sediments.” *Physics of Fluids*, 26(3), 35103.

Wang, R. Q., Adams, E. E., Law, A. W. K., and Lai, A. C. H. (2015). “Scaling Particle Cloud Dynamics: From Lab to Field.” *Journal of Hydraulic Engineering*, 141(7), 6015006.

Wu, L. H., Feng, D. J., Shimozono, T., and Okayasu, A. (2014). “Sediment Flux Measurement at High Concentration Based on Image Analysis with Combined Illumination.” *Journal of Japan Society of Civil Enginners Ser. B2 (Coastal Engineering)*, 70(2), 736–740.

Yoo, Y. J., Im, J. H., and Paik, J. K. (2014). “Flicker removal for CMOS wide dynamic range imaging based on alternating current component analysis.” *IEEE Transactions on Consumer Electronics*, 60(3), 294–301.

Yuan, Y. P., Avener, M. E., and Horner-Devine, A. R. (2011). “A two-color optical method for determining layer thickness in two interacting buoyant plumes.” *Experiments in Fluids*, 50(5), 1235–1245.

Zhao, B., Law, A. W. K., Adams, E. E., and Er, J. W. (2014). “Formation of particle clouds.” *Journal of Fluid Mechanics*, 746, 193–213.

Zhao, B., Law, A. W. K., Adams, E. E., Shao, D. D., and Huang, Z. H. (2012). “Effect of air release height on the formation of sediment thermals in water.” *Journal of Hydraulic Research*, 50(5), 532–540.

List of Tables

List of Figures

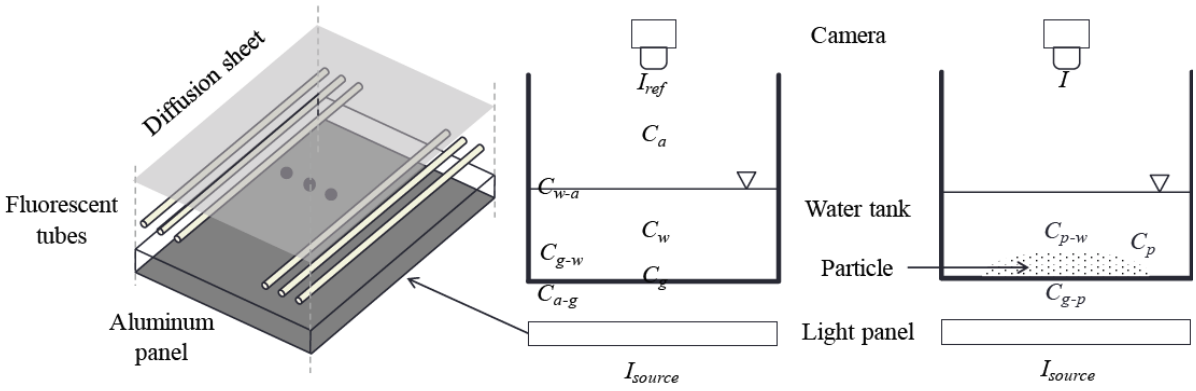

Fig. 1. Schematic diagram of the principle of LAM2D and experimental setup

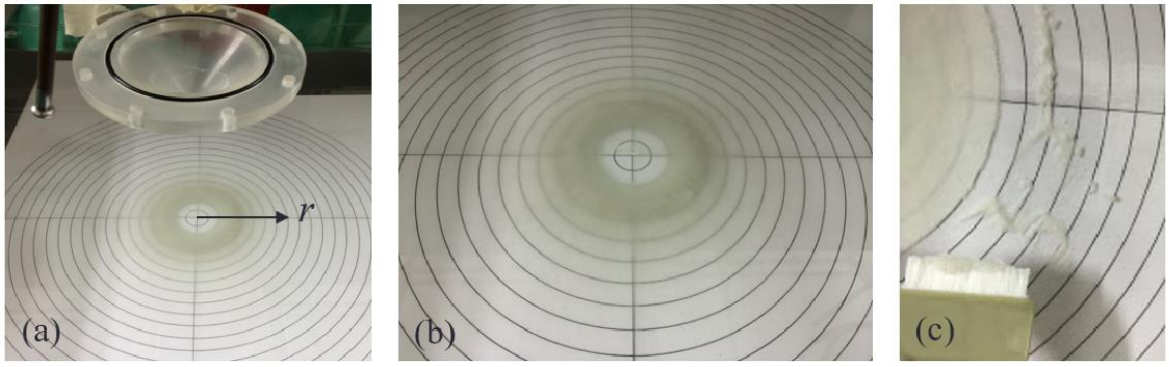

Fig. 2. Deposition of particle plume from five releases on a 10 mm grid space circular grid platform, (a) top view, (b) top view without funnel, and (c) sediment collection within grid with brush

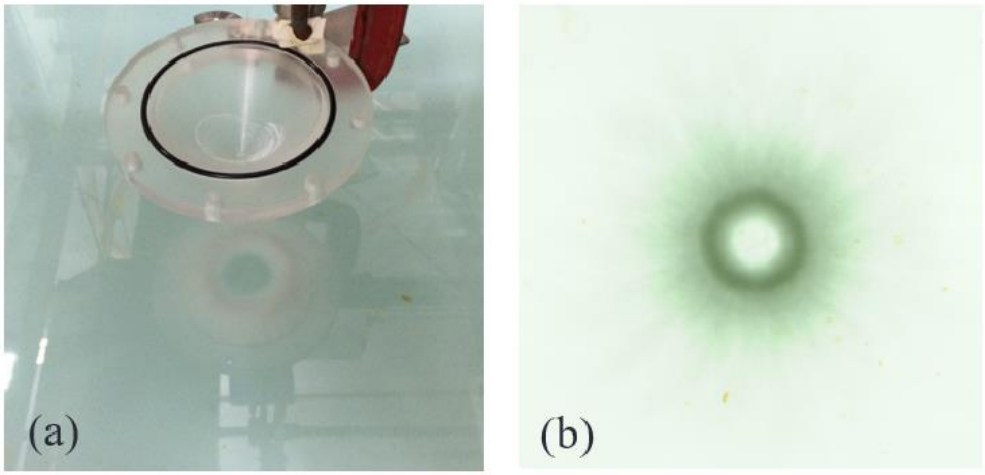

506

507 **Fig. 3.** Deposition of particle plume from five releases in water tank using backlighting with

508 light panel, (a) top view, and (b) top view without funnel

509

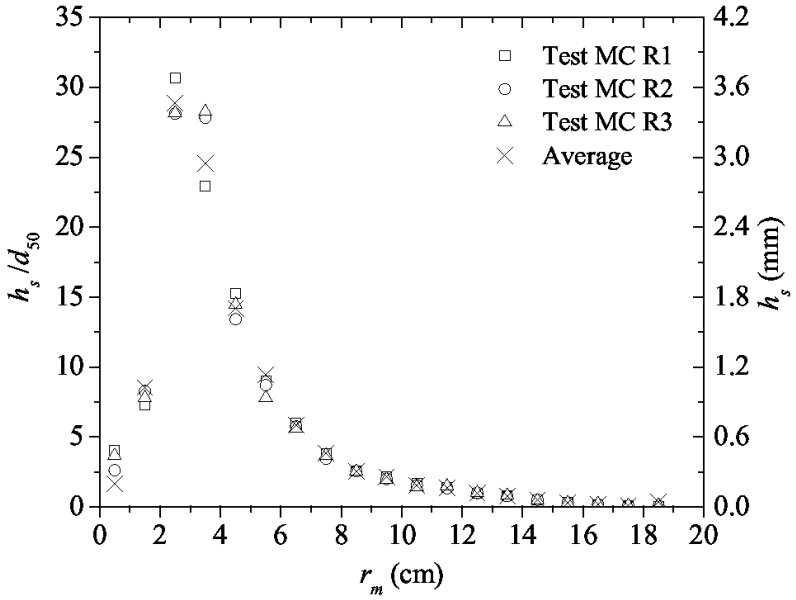

510

511 **Fig. 4.** Relationship between sediment depth, h_s/d_{50} and radius, r_m for three replicates of Test

512 MC (symbols) and averaged value (cross)

513

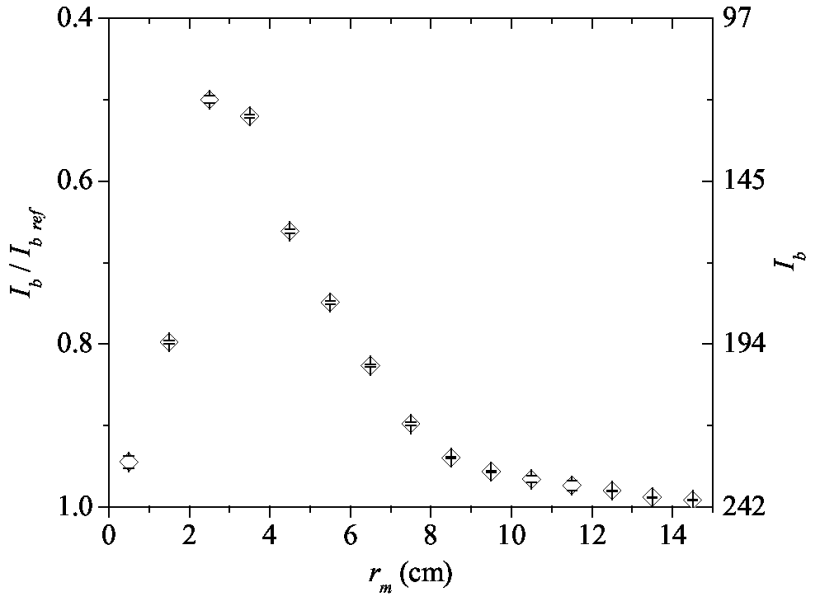

514

515 **Fig. 5.** Relationship between attenuated intensity, $I_b/I_{b\,ref}$ and radius, r_m

516

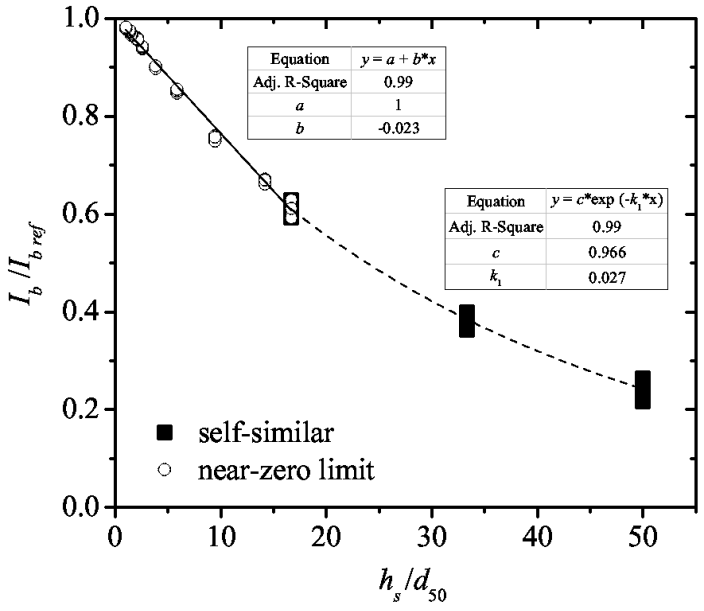

517

518 **Fig. 6.** Overall calibration curve

519

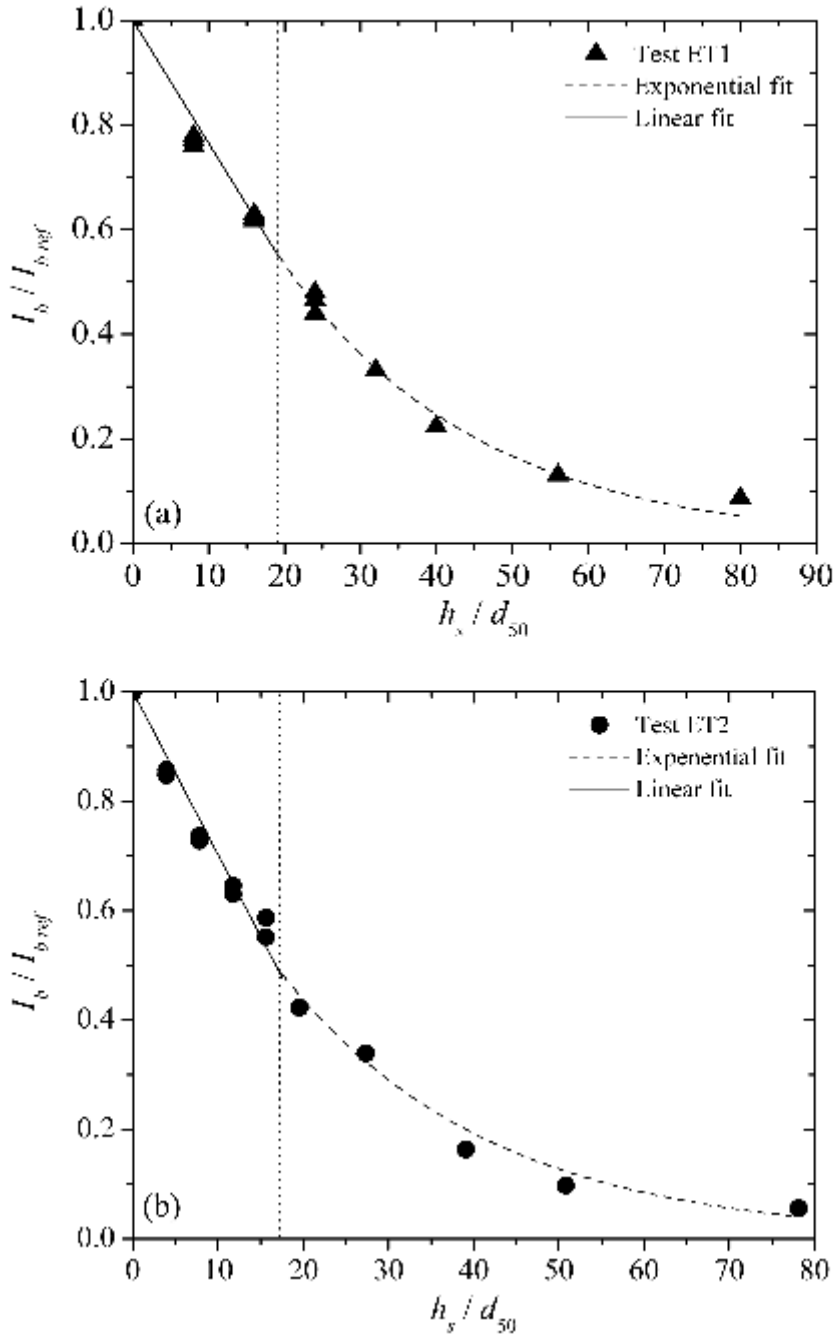

520

521 **Fig. 7.** Calibration curves from Tests (a) ET1 and (b) ET2. Note that, for smaller values of

522 h_s/d_{50}, up to three replicates were conducted in anticipation of greater experimental

523 variability in measurements at small h_s

524

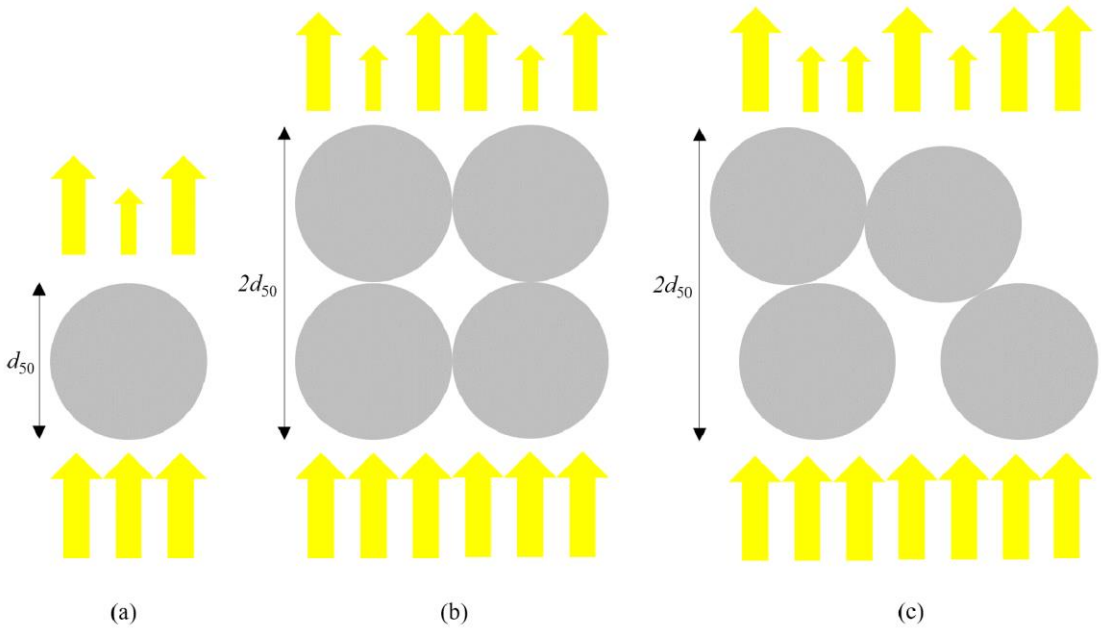

525

526 **Fig. 8.** Schematic diagram of light passing through (a) a single particle, and two layers of
527 particles with different packing configurations in (b) and (c). The size of arrows
528 represents the intensity of light

529

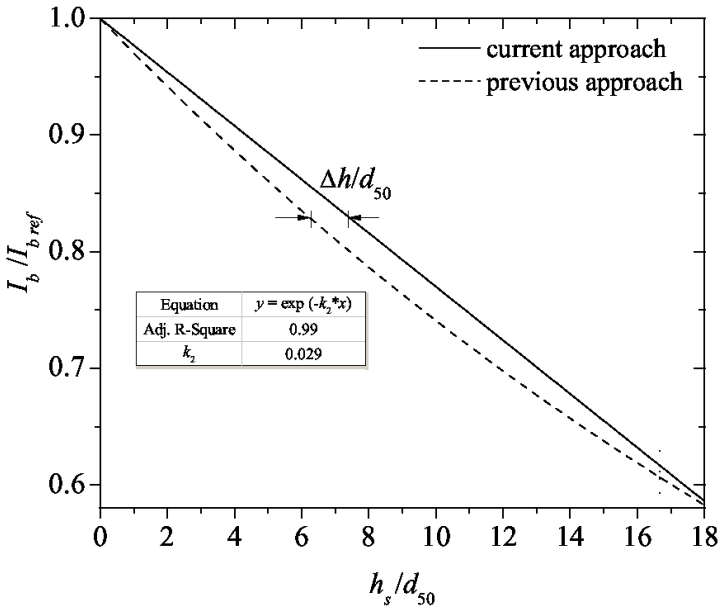

530

531 **Fig. 9.** Comparison of calibration curves in near-zero limit regime from current and previous
532 approaches

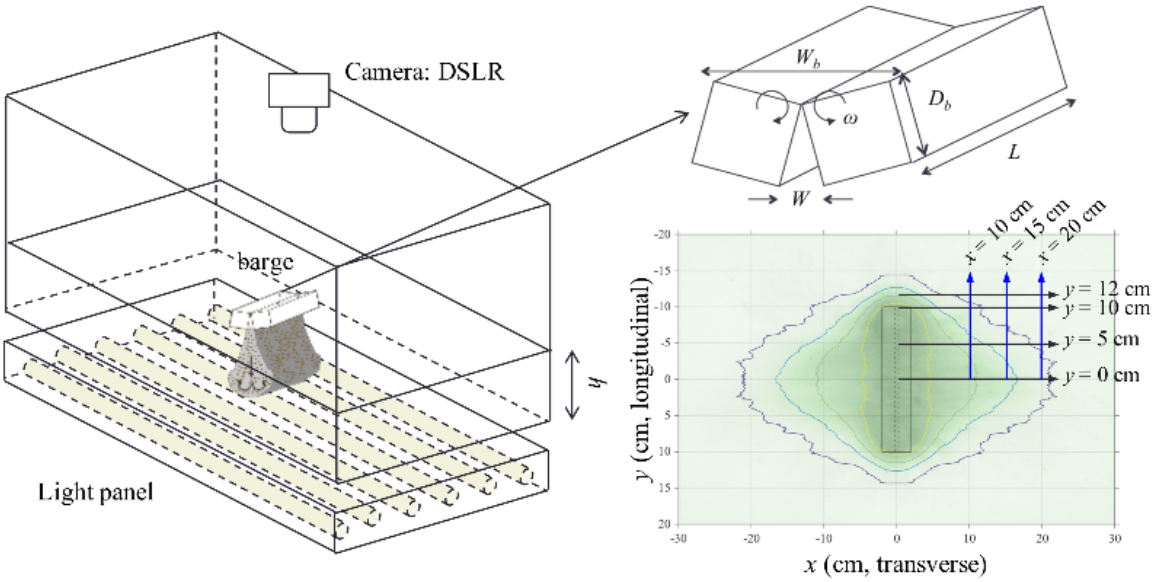

Fig. 10. Schematic diagram of model barge and illustration of deposition profiles at different cross-sections (lower right)

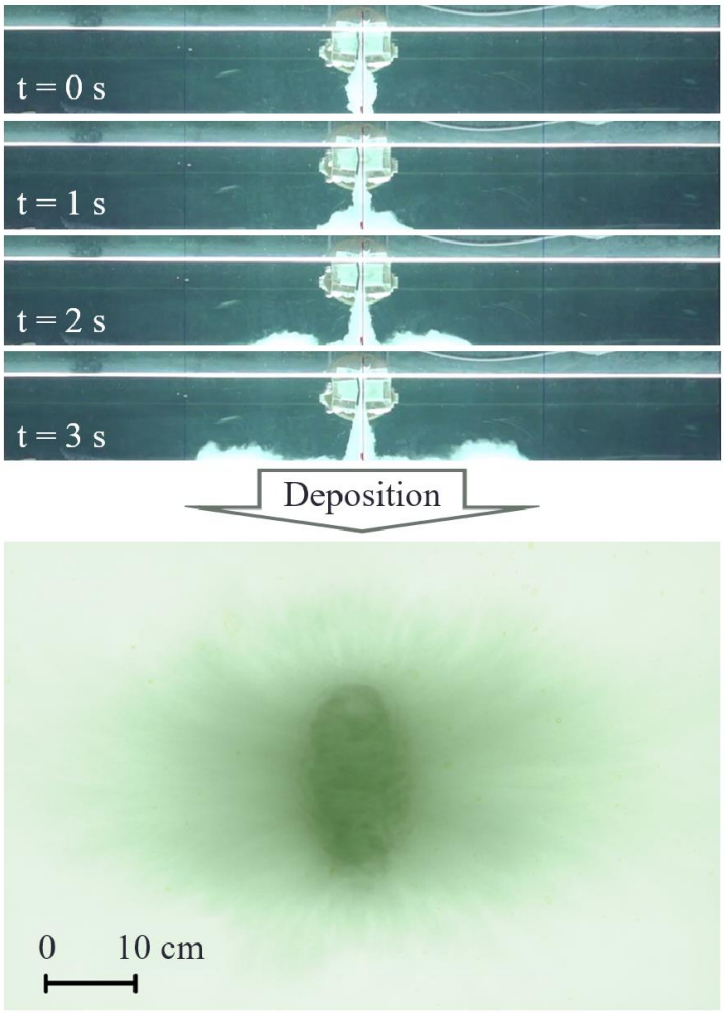

538

539 **Fig. 11.** Development of gravity currents and the deposition profile from barged sediments

540 disposal

541

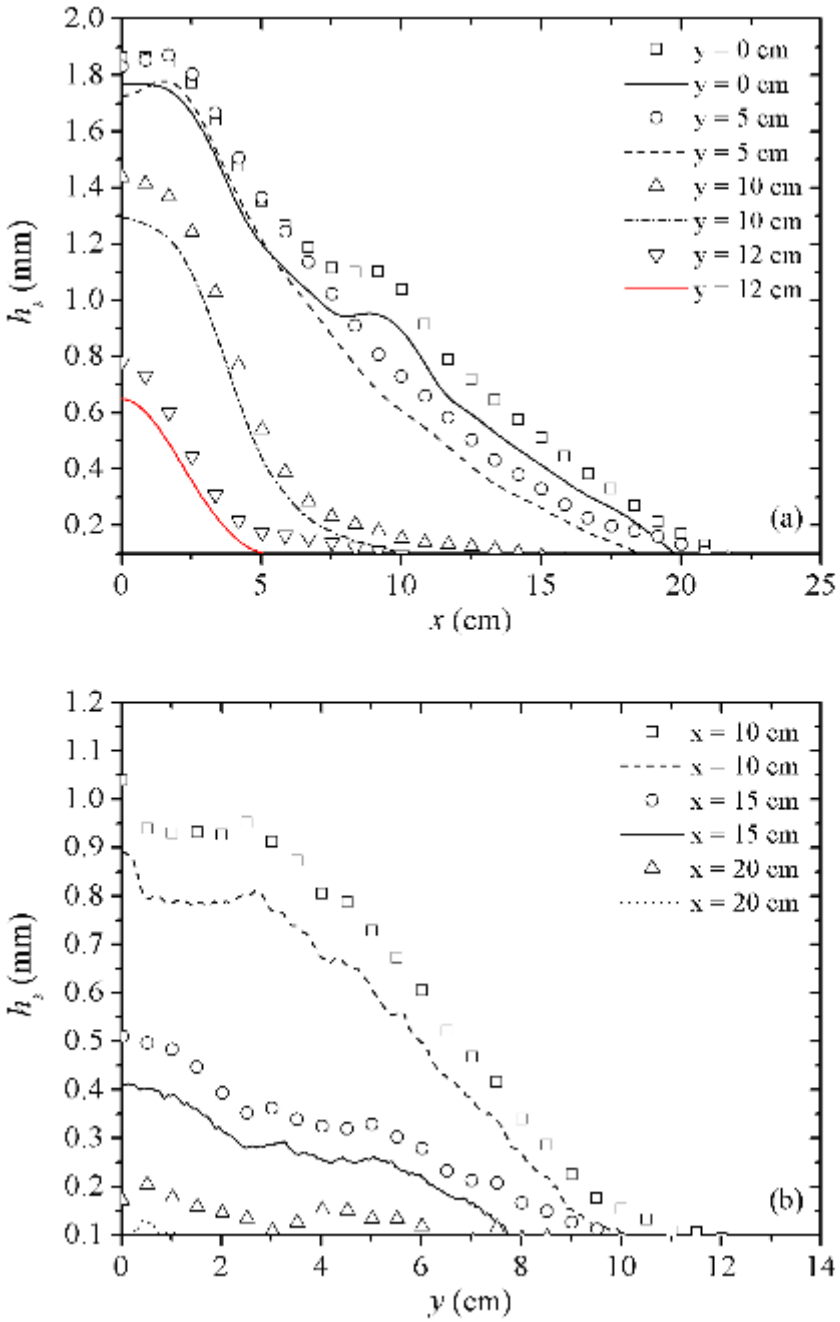

542

543 **Fig. 12.** Deposition profiles from barged sediment disposal (d_{50} = 0.12mm, L/W = 24) at (a)

544 y = 0, 5, 10 and 12 cm (longitudinal profile) and (b) x = 10, 15 and 20 cm

545 (transverse profile). Symbols denote current approach and lines denote previous

546 approach

547

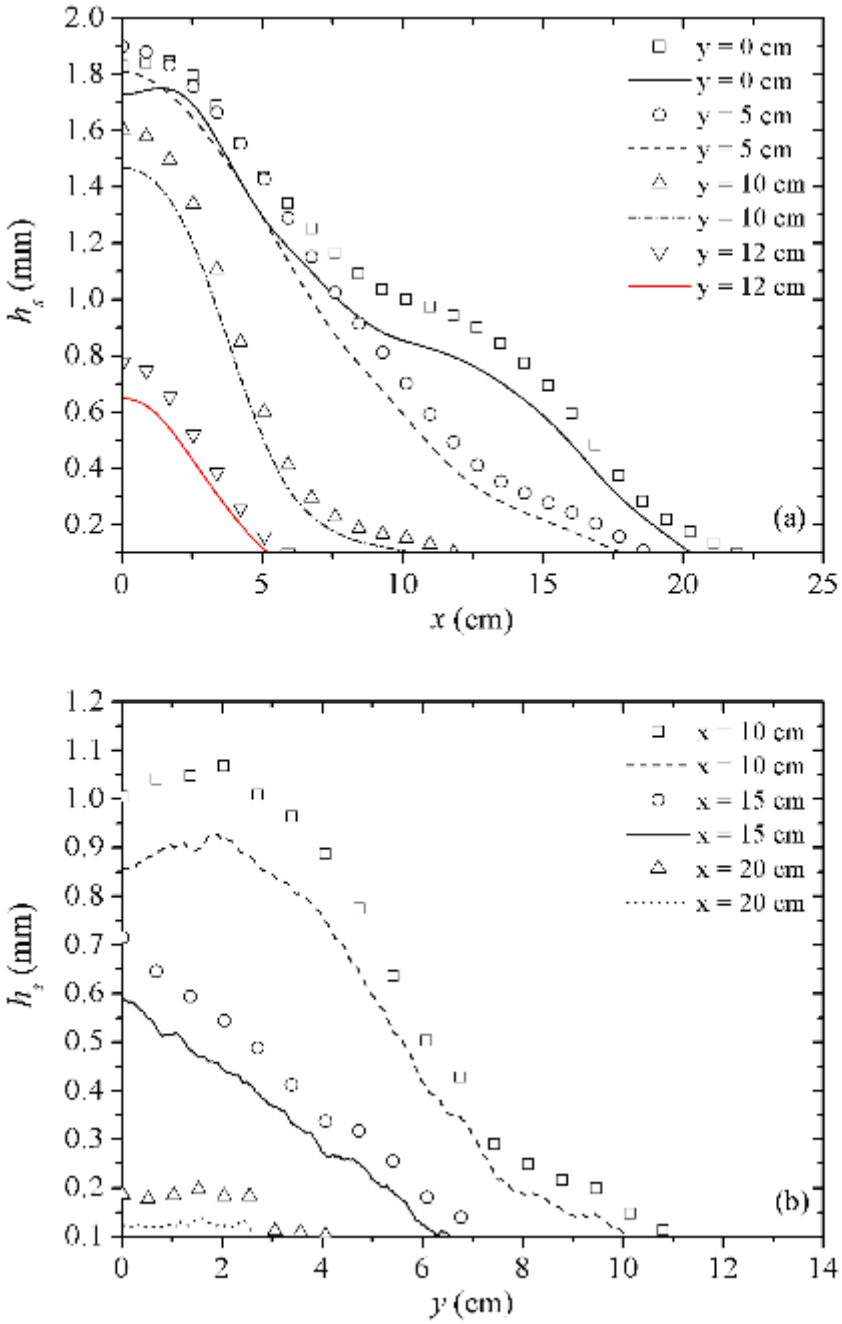

548

549 **Fig. 13.** Deposition profiles from barged sediment disposal (d_{50} = 0.12mm, L/W = 40) at (a)

550 y = 0, 5, 10 and 12 cm (longitudinal profile) and (b) x = 10, 15 and 20 cm

551 (transverse profile). Symbols denote current approach and lines denote previous

552 approach

553

Tables

Table 1. Criteria for the selection of DSLR camera parameters

Parameter	Description & Criteria
Exposure time, t_c	Duration of camera shutter opening to expose the sensor to the light. t_c to be higher than 1/40 to mitigate flicker
ISO Sensitivity	Ability of the sensor to capture light and convert into electrical signals for processing. Lowering the ISO value reduces the noise and hence is preferable for LAM2D
f-stops, *f*/*n*	Opening size of the aperture blades, which controls the amount of light entering the camera and affects the depth of field. Large *n* value is preferable to increase the depth of field
White Balance	Adjustment of the image color to match the real color, so that the color of the photo matches that observed visually

557 **Table 2.** Experimental conditions for particle plume deposition tests

Test	Mass per release (g)	Replicates	No. of releases	Remarks
MC	10	5	5	-
LA	10	5	5	R1 & R2 – day 1 R3 & R4 – day 2 R5 – day 3

558

559 **Table 3.** Experimental conditions for supplemental tests

Test	Size range (mm)	d_{50} (mm)	h_s (mm)	Range of h_s/d_{50}
ET1	0.21 ~ 0.30	0.25	2, 4, 6, 8, 10, 14, 20	8 – 80
ET2	0.43 ~ 0.60	0.51	2, 4, 6, 8, 10, 14, 20, 26, 40	4 – 78

560 Note: The number of replicates differed with h_s (varied from one to three), with thicker h_s
561 needing fewer replicates because experimental observations showed that variability decreased
562 when h_s increased